Diagnostic and Power Feed Upgrades to the MAIZE Facility

P. C. Campbell†, J. M. Woolstrum†, F. Antoulinakis†, T. M. Jones†, D. A. Yager-Elorriaga§, S. M. Miller†, N. M. Jordan†, Y. Y. Lau†, R. M. Gilgenbach†, and R. D. McBride†
†Department of Nuclear Engineering and Radiological Sciences, University of Michigan, Ann Arbor, MI 48109 USA
§Sandia National Laboratories, Albuquerque, NM 87123 USA

***Abstract*—The Michigan Accelerator for Inductive Z-pinch experiments (MAIZE) is a one stage, 1 MA, Linear Transformer Driver (LTD) at the University of Michigan. The MAIZE facility has been the site of various experimental studies, including wire array z-pinches for x-ray source development and cylindrical foil loads for implosion stability analysis. In order to better understand and investigate these and other experiments, a 4-frame extreme ultraviolet (EUV) camera was implemented, the optical stability of a 12-frame laser shadowgraphy system was improved, B-dot probes were upgraded, and a Rogowski coil was constructed. New conical load hardware was also developed to reduce the inductance of the transmission line and thus improve the current delivered to the loads.**

I. Introduction

PULSED Power Drivers are important devices in the study of plasma physics, particularly due to their applications in laboratory astrophysics [1], radiation generation [2], and fusion schemes such as magnetized liner inertial fusion (MagLIF) [3–6].

At the University of Michigan, a single-stage, 1 MA, Linear Transformer Driver (LTD) called MAIZE (Michigan Accelerator for Inductive Z-pinch Experiments [7, 8]) has been the driver for many experiments in liner implosion dynamics [9, 10] and radiation generation[11, 12]. While these experiments produced exciting results, they also highlighted the need for improved and additional diagnostics. In this paper, a new power feed, with a lower inductance and improved current delivery, will be discussed along with improvements in imaging and load current diagnostics.

II. Power Feed Upgrades

The MAIZE facility consists of a single-stage 0.1-Ω LTD capable of driving a 1-MA, 100-ns-risetime current pulse into a matched load. A cutaway view of the fully assembled machine is show in Fig. 1. The generator section consists of 40 bricks, each made up of two capacitors charged to opposite polarities, connected in series to a gas-filled spark-gap switch [13]. This section is connected to the load region through a coaxial-to-radial magnetically insulated transmission line (MITL). A 1-meter-diameter vacuum chamber houses the target, multiple diagnostics, and part of the transmission line.

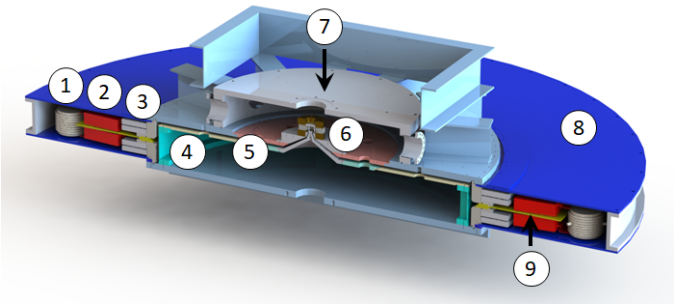

Fig. 1: A cutaway of the 3D model of MAIZE. (1) Spark-gap switch, (2) 40 nF capacitors, (3) iron core region, (4) coaxial transmission line section, (5) radial transmission line section, (6) load region, (7) vacuum chamber, (8) oil chamber, (9) high voltage insulator.

To improve the peak power on MAIZE, the load region transmission line was redesigned to have lower inductance. The newly designed conical power feed is shown in Fig. 2. It was designed to accommodate two large Helmholtz-like coils [14] as well as future and existing diagnostics.

To provide visual (line-of-sight) diagnostic access to the target, the target must be positioned (vertically) in line with the vacuum chamber ports. Consequently, the current must undergo some vertical translation upwards from MAIZE's capacitor plane to the target/diagnostics plane (see Figs. 1 and 2). Any vertical translation adds unwanted inductance to the system, which broadens the current pulse and reduces the peak power delivered to the load. For a given anode-cathode (A-K) gap spacing, the increase in inductance for a given combination of both radial and vertical translation is path dependent, and thus the path can be optimized to minimize the inductance of the overall power feed [15, 16]. However, a simple, straight conical feed yields an inductance that is reasonably close to that of an optimized, curved power feed. Thus, for simplicity, a conical feed was chosen for fabrication. In fact, two conical sections were implemented, in order to better accommodate the bottom Helmholtz-like coil (see Fig. 2).

The radius at which the radial feed transitions to the conical feed was varied to understand its effect on the overall system inductance. In general, the larger the transition radius, the lower the inductance. This can be seen in Fig. 3, which shows

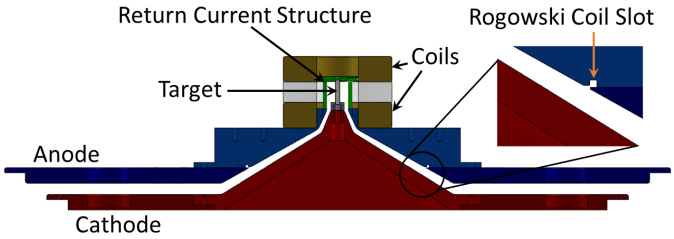

Fig. 2: An image of the new conical load hardware region on MAIZE showing the anode in blue (top electrode) and the cathode in red (bottom electrode). The target, e.g., a cylindrical foil liner (gray), is held in place at its top by a rigid connection made with the return-current structure (green). The bottom of the return-current structure is rigidly mounted to the upper surface of the anode. The bottom of the target slips into an aperture in a target-to-cathode adapter piece (dark gray). The target-to-cathode adapter rigidly mounts to the upper surface of the cathode. The slip-fit between the bottom of the target and the target-to-cathode adapter piece allows the vertical gap between the anode and cathode to decrease without crushing the target as the vacuum chamber is evacuated (this gap compression is $\sim$1 mm). Also shown are the Helmholtz-like coils (gold) surrounding the target region and the Rogowski coil slot cut into the anode structure. The Helmholtz-like coils enable an auxiliary magnetic field (on the order of a few tesla) to be applied to the targets, while the Rogowski coil is used to measure the total load current on MAIZE.

a plot of the total feed inductance (radial and conical) as a function of the transition radius. However, a larger transition radius also means a higher fabrication cost and a heavier, more cumbersome conical piece to handle during installation. To achieve a significant reduction in inductance while still being relatively easy to handle and fabricate, a transition radius of 15 cm was chosen for fabrication.

Another way to minimize the inductance is to use smaller A-K gaps. As shown in Fig. 3, a gap that tapers linearly from 1.3 cm to 0.5 cm in the conical section reduces the inductance by more than 4 nH relative to a constant 1.3-cm gap. A smaller gap is possible at the top of the conical feed due to the higher current density at the top of the feed. This higher current density provides the magnetic insulation to prevent shunt current losses in the power feed; if the gap were this small earlier in the power feed, then shunt current losses would be more likely due to the lower current density and larger inductive voltages at larger radii. Thus, we chose this tapering profile for fabrication (see Fig. 2).

The previous power feed on MAIZE was a tri-plate structure designed to enable side-on imaging of planar foil loads [17]. It was not designed for minimal inductance. A comparison of the load current obtained using the tri-plate and concial power feeds is provided in Fig. 4. The new cylindrically symmetric conical feed is also expected to deliver a more azimuthally uniform current pulse, relative to the previous tri-plate feed.

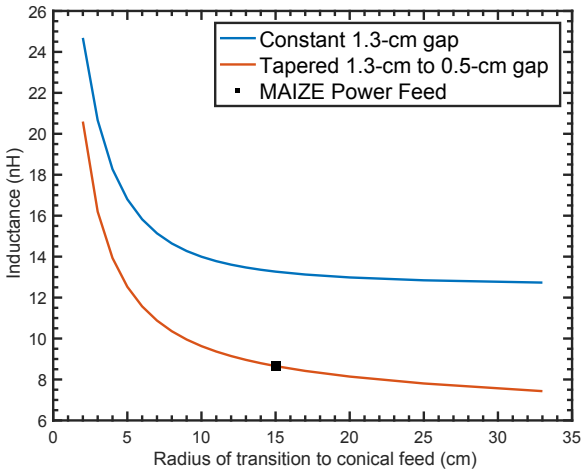

Fig. 3: A plot of inductance as a function of the radius where the pure radial feed transitions to the conical feed. Throughout these calculations, the outermost radius of the system (the outer radius of the radial transmission line segment) was held fixed at 33 cm. Also note that these scans included the inductance only up to the axial height that is flush with the uppermost surface of the blue anode structure shown in Fig. 2 (i.e., the inductance of the target and return-current structure was not included). The inductance and transition radius for the new tapered-gap power feed on MAIZE is also indicated (i.e., the inductance of 8.7 nH for a transition radius of 15 cm). The inductance of a target on MAIZE is in the range of 0.5–8 nH, depending on the target's radius and height. The initial inductance of a typical cylindrical foil target with a 3-mm initial radius and a 1-cm height [10] is about 3–4 nH. Thus, the total inductance on MAIZE (from a radius of 33 cm inward), with a typical cylindrical foil target installed, is about 12–13 nH.

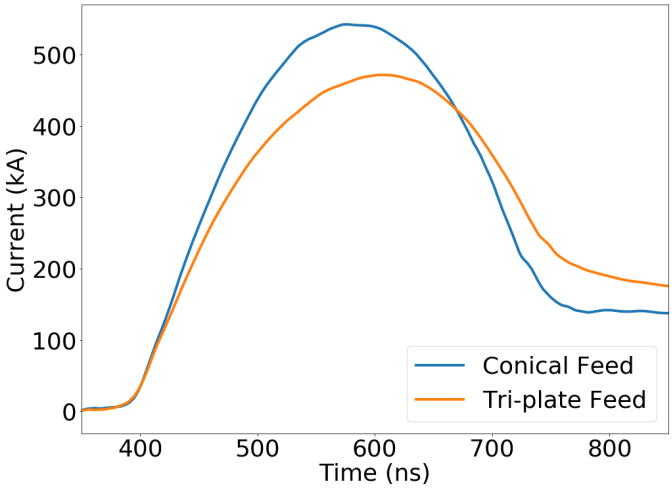

Fig. 4: Comparison of current pulses obtained using the same static (non-imploding) target on both the new conical feed and the old tri-plate feed. The conical feed increased the peak current by $\sim 10\%$ and reduced the rise time to peak current.

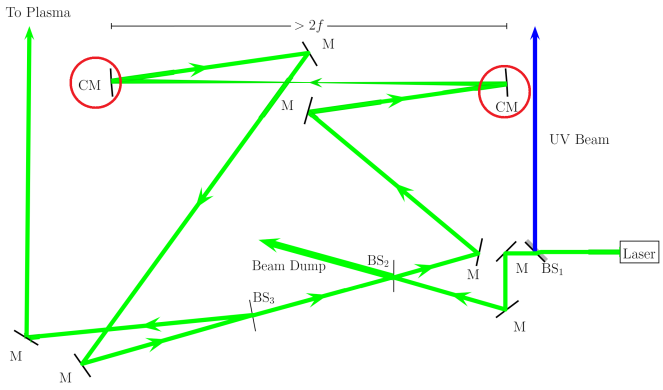

Fig. 5: The optical setup of the modified 12-frame shadowgraphy system. The beamsplitters (BS), planar mirrors (M), and concave mirrors (CM, circled in red) are indicated in the figure. This optical cavity configuration allows for 12 or more beams (delayed in time relative to one another) to share the same optical axis while maintaining stability.

III. Diagnostic Upgrades

A. Imaging Diagnostics

Imaging capabilities are essential for characterizing implosion dynamics and instability development. Consequently, improvements to the visible light laser shadowgraphy system have been made and a new extreme ultraviolet imaging system has been deployed.

1) Laser Shadowgraphy: The laser diagnostics on MAIZE make use of a single-pulse Nd:YAG laser source. The source outputs a fundamental 1064-nm beam (300 mJ), a frequency-doubled 532-nm beam (125 mJ), and a frequency-tripled 355-nm beam (80 mJ). The pulse lengths are 2 ns with 0.2 ns of jitter. For most of our laser diagnostics work, the 532-nm beam is used. In the near future, we will be using the UV beam for a deeper penetrating laser shadowgraphy and interferometry system. The fundamental 1064-nm beam is typically not used.

Complementing the laser is an intensified fast framing camera (the Invisible Vision Ultra UHSi 12/24), which is configured to record 12 image frames. The light collected for these images comes from a combination of both laser light (shadowgraphy) and plasma self emission. The fast framing camera's ICCD response curve is for visible light only. The exposure time for each frame is typically set to 10 ns.

In order to couple the fast 12-frame camera to a pulsed-laser shadowgraphy system, the single laser pulse must be split into 12 or more beams that are delayed in time relative to one another. This was previously accomplished using beamsplitters to allow the laser pulse(s) to enter and exit an optical cavity, as described in [9]. This system successfully generated 12 frames of shadowgraphy, but it was difficult to align due to the marginal stability of the cavity. Here we report on a modified setup (see Fig. 5), which has been implemented to improve both the optical cavity stability and the laser pulse uniformity across the multiple pulses/frames.

The diagram in Fig. 5 represents the physical layout of the optical components for the modified shadowgraphy system on MAIZE (though not drawn to scale). This physical representation is presented in order to highlight the importance of the incident and reflected angles on the concave mirrors—i.e., the incident and reflected optical axes must be nearly normal to the concave mirror surfaces (ideally to within less than 5°). If the angles become too large, then the beam's circular shape becomes elliptically distorted. The two flat mirrors in between the two concave mirrors are used to ensure these near-normal optical paths.

As with the previous setup [9], the modified setup reported here in Fig. 5 allows the 532-nm laser light to enter and exit the optical cavity through a 95/5 (transmission/reflection) beamsplitter. At a given point in space, each subsequent light pulse is delayed by 15 ns, which is set by the approximately 15-ft optical path length of the cavity. As the initial pulse enters the cavity, BS_2 (the first beamsplitter of the cavity) sends 95% of the beam energy to a beam dump, and BS_3 (the second beamsplitter of the cavity) picks off another 5% to send to the target. The intensity of each subsequent pulse is further reduced by about 10%. It is necessary to configure the beamsplitters this way in order to minimize the pulse-to-pulse intensity variation. If BS_2 were reversed, and it allowed 95% of the light to enter the cavity, each subsequent pulse would be 95% less intense than the previous pulse. Future diagnostics will use the "dumped beam" for interferometry and Faraday rotation measurements. As with the previous setup, the fast 12-frame camera is synchronized to capture the series of laser pulses directed from the optical cavity.

The stability of the new optical cavity may be calculated using the ray transfer (or ABCD) matrix of the overall system [18]. Each optical element in the system (e.g. mirrors, lenses, and the free space between the optics) has its own ray transfer matrix. For example, the transfer matrix for a curved mirror is given by

$$M_{cm} = \begin{pmatrix} 1 & 0 \\ -\frac{2}{R_e} & 1 \end{pmatrix}, \tag{1}$$

where R_e is the effective radius of curvature in the tangential plane. The matrices for each element are then multiplied together to result in a single ray transfer matrix for the system, M. Note that the order of the matrix multiplication is important, since matrix multiplication is non-commutative. From the product of the matrices, an eigenvalue equation may be solved to yield:

$$\lambda_{\pm} = g \pm \sqrt{g^2 - 1}, \;\; g = \frac{tr(M)}{2}, \tag{2}$$

where $\lambda_{\pm}$ are the eigenvalues, g is the stability parameter, and $tr(M)$ is the trace of the system transfer matrix M. The condition for stability is $g^2 \leq 1$ [18]. The two concave mirrors of the system each have a radius of curvature of 1000 mm, and they are separated by 1003 mm of free space. Upon multiplying the matrices together for every element in Fig. 5 (including the free space between every pair of elements in Fig. 5), we obtain $g^2 = 0.965$, and thus the system is stable.

A plot of MAIZE's stability parameter as a function of the distance between the concave mirrors is shown in Fig. 6. While the plot shows a wide range of distances over which the concave mirrors can be placed, their separation should be

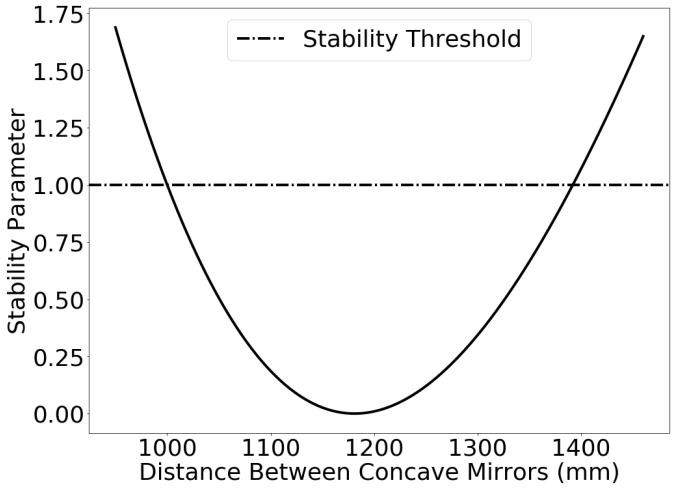

Fig. 6: The stability parameter g of the optical cavity plotted as a function of the distance between the concave mirrors. The threshold for stability ($g < 1$) is also plotted.

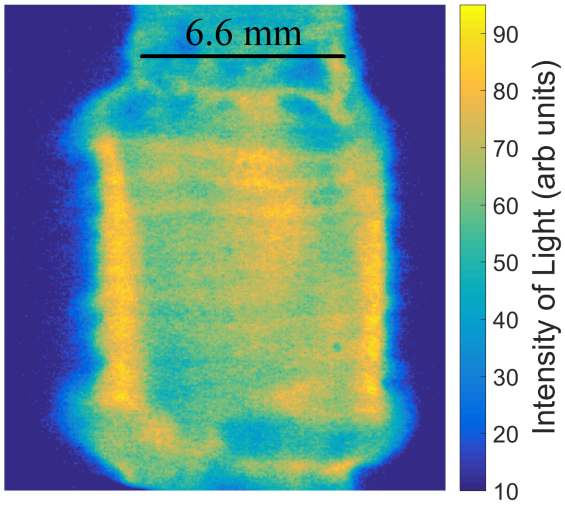

Fig. 7: A contrast-enhanced EUV camera image of an ablating 2-μm-thick aluminum liner.

as close as possible to 1000 mm to help preserve the original beam size. The farther apart the concave mirrors are placed, the smaller each subsequent beam in the optical cavity becomes. Another way of looking at this is that since this setup makes use of two concave mirrors separated by a distance of $\gtrapprox 2f$, where $f \approx R_e/2$ is the focal length of the concave mirrors, the cavity is in a region of optical stability.

An alternative to using a pulsed laser coupled to an optical cavity for 12-frame shadowgraphy is to simply use a continuous-wave (CW) laser, which removes the need for the optical cavity. Indeed, our laboratory is pursuing this option and is presently in the process of acquiring a 6-W, 532-nm CW laser. This will allow us to easily change the inter-frame times of the 12-frame (or even 24-frame) laser shadowgraphy system. Note that with a pulsed laser coupled to an optical cavity, changing the inter-frame times requires a lengthening of the cavity's optical path, which can be exceedingly cumbersome. However, there are advantages to using a pulsed laser coupled to an optical cavity for many experimental situations. First, the intensity is typically much higher for pulsed lasers when compared to CW lasers. This is an important factor to consider when the plasma is strongly radiating at the laser wavelength (as in a typical MAIZE experiment). Without sufficient laser intensity, the self-emission of the plasma will dominate the image, greatly reducing the shadowgraphy contrast. Second, pulsed lasers are potentially safer for the ICCD camera. For example, if the camera shutter is inadvertently left open, a CW laser could damage the camera's ICCD, as the deposited laser energy will accumulate over time. To mitigate the risk of a CW laser damaging the ICCD, multiple optical shutters should be used for redundant protection (i.e., in case one of the shutters fails to close, there are other shutters which hopefully do close). Finally, the time resolution of a shadowgraphy system is determined by whichever is shorter, the laser pulse length or the frame exposure duration of the camera. On MAIZE, the fast-framing camera is capable of 5-ns exposures, while the laser has a 2-ns pulse duration. With a shorter-pulse laser, even better time resolution could be achieved.

2) Extreme Ultraviolet (EUV) Camera: In addition to the improved laser shadowgraphy system, a time-gated, four-frame EUV pinhole camera has been implemented. The system uses ∼100-μm pinholes placed approximately halfway between the load region (the object plane) and the camera detector (the image plane). The resulting image magnification is $M \approx 0.92$. The camera's detector is sensitive to photons above ∼7 eV [19]. A sample image from the system is presented in Fig. 7.

Each of the four frames has a variable 5–20 ns exposure, with a 15-ns inter-frame delay. Additionally, the line of sight of the EUV camera is perpendicular to the optical shadowgraphy setup, so two different regions of the liner can be imaged simultaneously. This helps when trying to correlate instability structures that wrap around the imploding cylindrical liner (this is particularly helpful when the instability structures are helical [10]).

Following Ref. [19], the geometric resolution of the system is given by

$$L_{\text{geo}} = d\left(1 + \frac{p}{q}\right), \tag{3}$$

where d is the diameter of the pinhole, p is the object-to-pinhole distance, and q is the pinhole-to-image distance. For the system on MAIZE, $d = 100$ μm, $p = 0.61$ m, and $q = 0.56$ m, which gives $L_{\text{geo}} = 209$ μm. The inherent resolution of the microchannel plate (MCP) detectors in the EUV camera is ∼100 μm. The system's geometric resolution can be improved by switching to smaller pinholes (d), decreasing the object-to-image distance (p), and/or increasing the pinhole-to-image distance (q). However, because of diffraction limitations, decreasing the pinhole size also decreases the number of UV photons that reach the camera detector. For example, the diffraction limited spatial resolution is given by

$$L_{\text{diff}} = 1.22\frac{\lambda p}{d}, \tag{4}$$

where λ is the wavelength of the imaging photons. For 100-μm pinholes, $L_{\text{geo}} \geq L_{\text{diff}}$ only when $h\nu \geq 45$ eV.

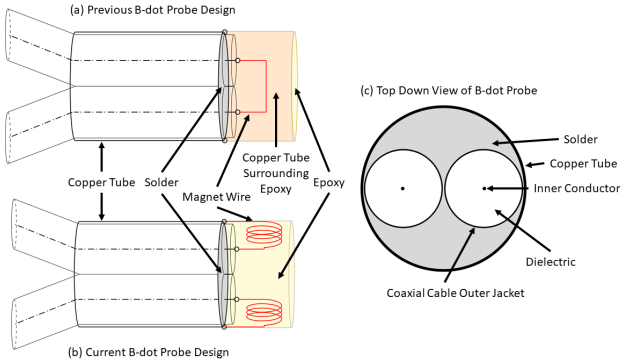

Fig. 8: (a) The previous B-dot probe design on MAIZE. The magnet wire (red) is soldered to the inner conductors of two adjacent semi-rigid coaxial cables, forming one single-turn loop. The outer conductors of the two coaxial cables are soldered together, and the loop of magnet wire is held in place by non-conductive epoxy, which is surrounded by a copper tube. (b) The new B-dot probe design on MAIZE. The magnet wire (red) is soldered to the inner and outer conductors of the two coaxial cables. The outer conductors of the two coaxial cables are soldered together, and the loops of magnet wire are held in place by non-conductive epoxy. (c) A top down view of the B-dot probes in (a) and (b) in the plane of the solder's outer surface (gray).

For 50-μm pinholes ($L_{\text{geo}} = 104$ μm), this threshold instead occurs at $h\nu \geq 180$ eV. If the only photons being generated by the plasma are 45-eV photons, then the 50-μm-pinhole system resolution will be limited (and actually degraded relative to the 100-μm-pinhole case) by diffraction (i.e., $L_{\text{system}} = L_{\text{diff}} = 411$ μm); however, if the plasma is hot enough to be generating significant amounts of 180-eV photons, then the better geometric resolution might be accessible (i.e., $L_{\text{system}} = L_{\text{geo}} = 104$ μm). Finding the right pinhole sizes for the emission characteristics of a particular plasma source usually requires some experimentation.

B. Current Diagnostics

Accurate magnetic field and current measurements are essential to understanding the magnetic drive pressure that is applied to a target during an experiment. These measurements are often made with B-dot probes and Rogowski coils.

1) B-dot Probes: Previously, the only current diagnostics fielded on MAIZE were B-dot probes. The B-dot probes are situated at a radius of 44 cm from the center of the target chamber, in four locations that are spaced evenly in the azimuthal direction. This allows each B-dot to monitor the current flowing through one quadrant of the LTD, which is useful for determining the azimuthal current distribution in the LTD. These B-dot probes (see Fig. 8(a)) were successful for determining the current on MAIZE for many years. However, because of accumulated damage, they needed to be replaced.

The newly redesigned B-dot probe packages (two B-dot sensors per package—see Fig. 8(b)) were constructed as follows: (1) The ends of two semi-rigid coaxial cables were stripped, exposing the center conductors on both ends of both cables. (2) The outer conductors of the two cables were soldered together, forming a cable pair. (3) The cable pair was inserted into a copper tube (when installed in MAIZE, this copper tube makes an electrical contact with the feed anode). (4) The sensor end of the copper tube was filled with solder (the outer surface of the solder is represented by the gray-filled circles in Fig. 8). From experimentation, we found that this solder is necessary to obtain reliable dB/dt signals. (5) Insulated magnet wires were attached to the exposed center conductors on the magnetic field sensing end of each cable. (6) The free ends of the magnet wires were soldered to the outer conductors after first being wrapped into three-turn pickup loops, with loop diameters of 1.68 mm. The pickup loops are wrapped in opposing directions, to produce signals of opposite polarity. (7) The pickup loops are covered in non-conducting epoxy to keep them in place and to help prevent charge buildup on the magnet wire. (8) On the output end of the probe package, the coaxial cable was 50 mm long; this length was chosen to facilitate soldering the coaxial cable to SMA connectors.

Both the previous and new B-dot packages made use of differential measuring techniques to reject common-mode noise. That is, the packages output two signals of opposite polarity, where the difference between the two recorded signals, divided by 2, is the common-mode-rejected signal of interest (see Fig. 9). Relative to the previous design, the new design was aimed at increasing the overall probe sensitivity and signal-to-noise ratio; thus, the new design uses two three-turn loops instead of one single-turn loop. The signal-to-noise ratios for the new design is 11.0 dBc, whereas the ratio for the previous design was 1.5 dBc.

Ideally, the signal voltage from a B-dot probe can be calculated from $V = -Nd\Phi_B/dt$, where N is the number of wire loops, and Φ_B is the magnetic flux that penetrates the conducting wire loops. In MAIZE, the time-changing magnetic flux is produced by the time-changing current pulse in the transmission line. In reality, magnetic flux penetration into conducting materials takes time. Taking the characteristic flux penetration time τ_f into consideration, the current in the MAIZE transmission line can be calculated using [20]

$$I = C \cdot e^{-t/\tau_f} \int_0^t V_B \, e^{t/\tau_f} \, dt, \tag{5}$$

where C is the probe's calibration constant in units of A/(V·s), and V_B is the probe's recorded signal voltage. Note that t = 0 should correspond to the start of current. In Fig. 10, a representative experimental current trace is plotted along with the corresponding simulated trace.

The B-dot probes are calibrated *in situ* on MAIZE. This is done by operating MAIZE with a known, constant-impedance load that is well matched to the characteristic impedance of MAIZE. The recorded B-dot signals are then scaled to match the output from a validated circuit model of MAIZE [12]. This model takes into account the lumped resistance, inductance, and capacitance of MAIZE's vacuum cavity and 40 parallel bricks. This model also accounts for the power losses that result from the eddy currents in MAIZE's ferromagnetic cores. (Note that the B-dot probes are also roughly calibrated using

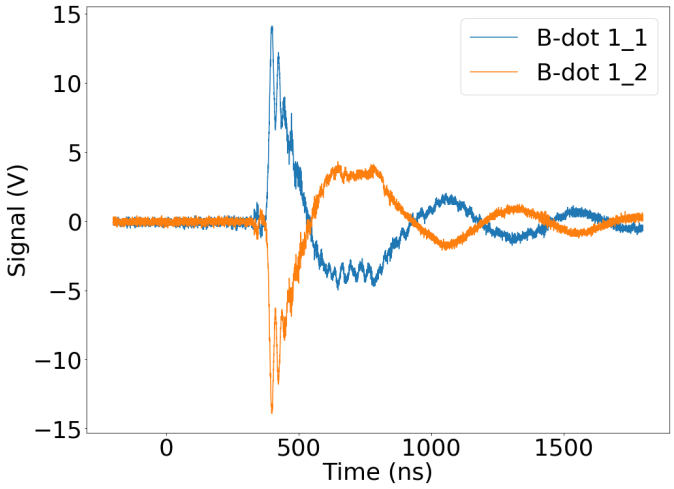

Fig. 9: Unprocessed signals from the new B-dot package of Fig. 8(b). The two curves are from the package's two outputs.

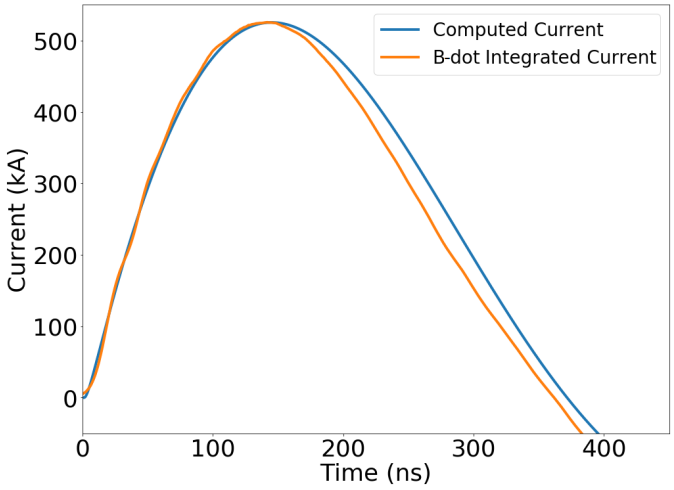

Fig. 10: Measured and simulated load current on MAIZE. The measured current was obtained by integrating the B-dot signals in Fig. 9, which were obtained using the new B-dot package of Fig. 8(b).

a table-top mini-pulser prior to being installed in MAIZE; this table-top test provides a sanity check for the *in situ* calibration.)

2) Rogowski Coil: Rogowski coils are also used to make current measurements [21]. They operate in a similar manner to B-dot probes, where the voltage induced is proportional to the time derivative of the magnetic flux penetrating the coil, which is proportional to the time derivative of the current. Rogowski coils, however, are helical/toroidal coils, with a minor loop radius and a major loop radius. Because of their winding geometry, Rogowski coils measure the total current flowing through the major loop, and (if properly constructed) the measurement is insensitive to where the current is flowing within the major loop [21]. The voltage induced on a Rogowski coil can be calculated using

$$V(t) = \frac{-AN\mu_0}{\ell}\frac{dI(t)}{dt}, \tag{6}$$

where A is the area of the minor loops, N is the number of minor loops, and ℓ is the length of the Rogowski coil (i.e. the circumference of the major loop).

The four B-dot probes on MAIZE provide information about the azimuthal symmetry of the power delivery. However, any shunt current losses occurring downstream of the B-dot probes (i.e., between the B-dot probes and the load) spoils the ability of the B-dot probes to measure the total current delivered to the load. Relative to the location of the B-dot probes, the Rogowski coil on MAIZE is located much closer to the load to obtain a more reliable measurement of the total current delivered to the load (see Fig. 2).

The Rogowski coil on MAIZE was fabricated by etching away part of the outer conductor of a semi-rigid coaxial cable to produce a helical outer conductor. At one end of the cable, the cable's center conductor was soldered to the outer helical conductor; at the other end of the cable, the cable's inner and outer conductors were soldered to an SMA connector. The cable was then wrapped into the toroidal shape of a Rogowski coil. This fabrication technique was inspired by that of the Rogowski coil used on the COBRA facility at Cornell University [22].

The diameter of the semi-rigid coaxial cable (1.68 mm) was chosen to minimize the voltage that the Rogowski coil would generate during an experiment on MAIZE. Pin-striping tape (1/8 inch wide) was wound helically around the cable for 34 evenly spaced turns to create a mask for the etching solution. After the pin-striping tape was applied, the cable was placed in a tub of etching solution (hydrocholoric acid and hydrogen peroxide) for several hours. This leaves a helical band of outer conductor (copper) surrounding the cable's dielectric insulator (see Fig. 11). Once the etching process was complete, the inner conductor was soldered to the helical outer conductor at one end of the cable and soldered to an SMA connector at the other end of the cable. The cable was then shrink wrapped with insulating material and installed in the anode of MAIZE's new conical power feed. The output voltage of the Rogowski coil on MAIZE was estimated to be $\sim$1 kV. Thus, 9 dB of inline attenuation was added to reduce the possibility of electrical breakdowns occurring in subsequent signal routing components.

The Rogowski coil was calibrated while residing in MAIZE's new conical power feed hardware (*cf.* Figs. 2 and 11). A simple pulse generator, composed of a capacitor and a spark-gap switch, sent an approximately 3-kA current pulse through a cable that was connected to the hardware. This cable also passed through a Pearson coil, which was used as the calibration standard. From the two signals, the Rogowski coil's calibration factor was determined.

In Fig. 12, we present example current traces as measured by the Rogowski coil and the average of the four B-dot probes. The two current diagnostics show similar pulse characteristics and measure the peak current to within 10% of each other. The discrepancy is likely due to the uncertainty in the resistance value assumed for the static load when calibrating the B-dot probes. As mentioned above, the B-dot probes are calibrated *in situ* on MAIZE using a static-impedance load and a circuit model [12]. The circuit model requires (as input parameters)

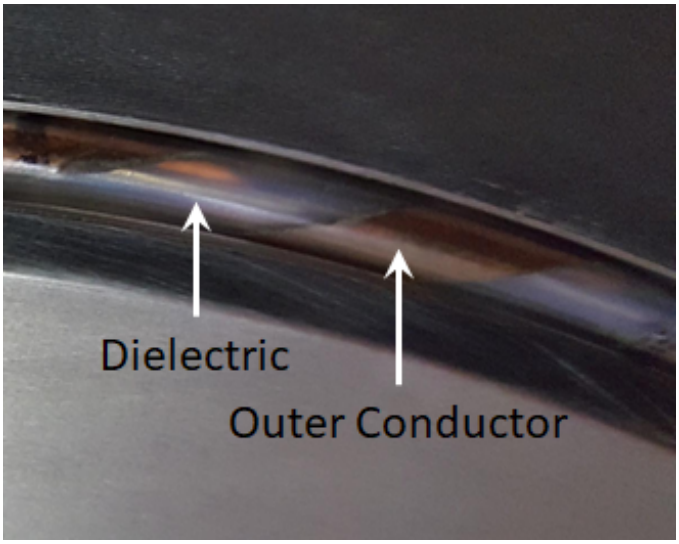

Fig. 11: A photograph of a section of the MAIZE Rogowski coil installed in the anode slot of MAIZE's new conical power feed (*cf.* Fig. 2). The insulating dielectric of the semi-rigid coaxial cable is apparent where the cable's outer conductor (copper) has been etched away. The copper forms a helical band around the dielectric.

known values for the resistance and inductance of the static-impedance load. For this reason, we take the current as determined by Rogowski coil to be the more direct and reliable measurement.

Another difference observed between the Rogowski signal and the average B-dot signal in Fig. 12 is the time at which the two signals "flatline." This flatlining occurs just after peak current for the Rogowski coil and almost 100 ns after peak current for the B-dot probes. The flatlining is likely an indication of plasma in the A-K gap of the machine. This plasma could potentially cause a flatlined signal via several mechanisms. One mechanism is that the plasma could simply damage the probes, causing the probes to output zero voltage, and thus the integrated dB/dt signals would appear as flat lines. We do not believe that this mechanism applies to our case, since our probes survive from shot to shot. Another possibility is that the plasma could crowbar the load current (short out the load current) at a machine radius that is larger than the radial location of the current measurements. In this case, the current measurements would be properly indicating a non-changing (or, more precisely, a slightly decaying) magnetic field at their locations. The decay time is the L/R decay time of the magnetic flux trapped between the load and the radial location of the crowbar. A third possibility is that the plasma encapsulates the probe sensors and thus shields the probes from fully sensing the temporal changes in the driving magnetic field. Presently, we do not have an appropriate diagnostic capability to detect or characterize such a plasma in our power feed, but we are working to develop one for the near future.

Our hypothesis as to why plasma would be present at the two different measurement locations at two different times has to do with the fact that, in the A-K gap, both the power flow and plasma flow reverse directions after voltage reversal, and voltage reversal occurs immediately after peak current (since $V \approx L\dot{I}$). That is, before and after peak current, the magnetic field $\mathbf{B}$ is in the same azimuthal direction. However, the direction of the electric field $\mathbf{E}$ changes sign after peak current, since $E \approx V/d$, where d is the A-K gap spacing. Thus, both the electromagnetic energy flux (i.e., the Poynting vector $\mathbf{S} = \mathbf{E} \times \mathbf{B}/\mu_0$) and the charged particle drift velocity ($\mathbf{v}_{\rm drift} = \mathbf{E} \times \mathbf{B}/B^2$) reverse directions after peak current (from radially inward to radially outward) [23].

The system power reversal can do two things: (1) it can source plasma from metal electrodes due to the inverse skin effect [24, 25]; and (2) it can cause the sourced plasma to flow radially outward at the drift velocity $\mathbf{v}_{\rm drift} = \mathbf{E}\times\mathbf{B}/B^2$. When the Poynting vector is pointed radially inward, magnetic flux is driven into the system, including into the bulk of the metal electrodes and the metal load, due to resistive diffusion. After peak current, the Poynting vector reverses, and magnetic flux is pulled out of the system. As the current begins to decrease, the magnetic field at the metal-vacuum interface can decrease faster than the magnetic field inside of the metal, because it takes time for the decreasing vacuum magnetic field to diffuse into the metal. Thus, the magnetic pressure $p_{\rm mag} = B^2/(2\mu_0)$ in the vacuum can become lower than the magnetic pressure in the metal. This can cause the outer layers of the metal (near the metal surface) to explode outwards, into the A-K gap. Since the magnetic pressure is $p_{\rm mag} = B^2/(2\mu_0) \propto I^2/r^2$ (with $B = \mu_0 I/(2\pi r)$), the largest variations in magnetic pressure will occur at the smallest radii in the system, which is near the load, where the most intense ohmic heating also takes place (due to the large current densities). Therefore, the inverse skin effect could be the source of plasma in the A-K gap, which begins near the load and then propagates radially outward, first passing by the Rogowski probe and later passing by the B-dot probes (100 ns later, according to Fig. 12).

For a simple order-of-magnitude estimate of $\mathbf{v}_{\rm drift} = \mathbf{E} \times \mathbf{B}/B^2$, we first note that the LTD's voltage and current waveforms are both approximately sinusoidal and 90° out of phase with each other, since $V = L\dot{I}$. We also note that the drift velocity is not constant in space or time. The magnitude of the drift velocity ($v_{\rm drift} = E/B$) is larger at larger radii, where the electric field (voltage) is higher and the magnetic field is lower. Furthermore, at peak current, the voltage is approximately zero (since $V \approx L\dot{I}$). This means that $\mathbf{E} \approx 0$, and thus $\mathbf{v}_{\rm drift} \approx 0$ at peak current. However, according to Fig. 12, the time when the B-dot probes flatline is approximately 100 ns after peak current (at $t \approx 700$ ns). At this time, the LTD's approximately sinusoidal voltage waveform is at about -45 kV for a radial location of 27.5 cm. The radial location of 27.5 cm was selected because it is halfway between the radius of the Rogowski coil (11 cm) and the radius of the B-dot probes (44 cm). The voltage of -45 kV was found using $V = L\dot{I}$, where $L \approx 12$ nH is the inductance of the load and the power feed up to the radial location of 27.5 cm. Since the voltage varies nearly linearly with time, from approximately zero volts to -45 kV over the time period of interest, we simply use the mean value of -22.5 kV. Applying -22.5 kV

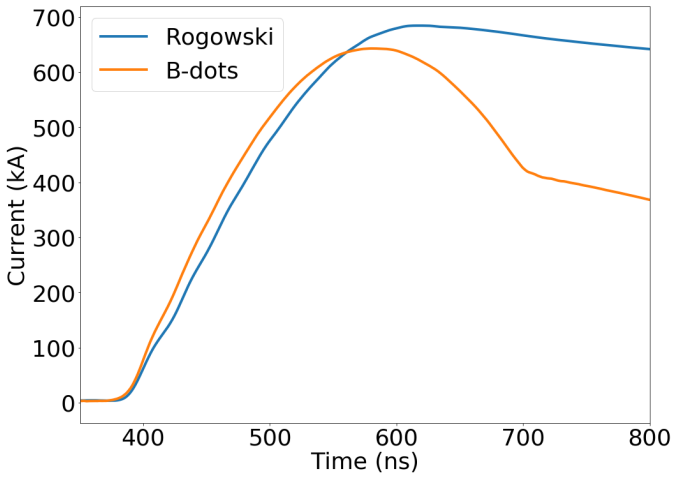

Fig. 12: A sample trace of the currents from both diagnostics for a short circuit load.

across the 1.3-cm vertical A-K gap of the radial portion of the MAIZE power feed, we get $E \approx -1.7 \times 10^6$ V/m. Similarly, the B-dot current at the halfway point of our time period of interest is about 575 kA. Applying 575 kA and $r = 27.5$ cm to $\mu_0 I/(2\pi r)$ gives $B \approx 0.4$ T. Therefore, $v_{\text{drift}} = E/B \approx 4.1 \times 10^6$ m/s in the radially outward direction. The radial distance from the Rogowski coil to the B-dot probes is $\Delta r = 44 - 11 = 33$ cm. Thus, the time to travel this distance is $\Delta t = \Delta r / v_{\text{drift}} \approx 80$ ns, which agrees reasonably well with the observed difference of about 100 ns.

IV. Conclusions and Future Work

A new conical power feed and several diagnostic upgrades have been implemented on the MAIZE facility. With these upgrades, new experiments will be conducted with improved current delivery and diagnostic information. Experiments to investigate liner implosion dynamics, driver-target coupling (power flow), and neutron radiation sources (deuterium pinches) are of particular interest. Additionally, collaborative efforts to investigate x-ray sources, warm dense matter, and laboratory astrophysics will be supported. Diagnostic development will remain a priority as well. Diagnostic development projects presently underway include X-pinch-based point-projection x-ray radiography [26, 27], visible spectroscopy, UV and visible laser-based interferometry and Faraday rotation, and the addition of a 532-nm, 6-W, CW laser for laser probing on variable/flexible time scales. Additionally, a bolometer, photoconducting diamond detectors (PCDs), and silicon diodes are now available for diagnosing x-ray generation.

Acknowledgment

We would like to thank two Referees for carefully reviewing our manuscript and for providing helpful suggestions. We thank Dr. Matthew Gomez for useful discussions regarding the B-dot probe design. We thank Dr. Jon Douglass, Dr. John Greenly, Prof. Pierre Gourdain, and Harry Wilhelm for useful discussions regarding the Rogowski coil. We thank Prof. Pierre Gourdain for useful discussions regarding the EUV camera. We thank the Applied B on Z (ABZ) team at Sandia National Laboratories for donating the Helmholtz-like magnetic field coils on MAIZE. We thank Dr. Michael Jones and Robert Hohlfelder for donating the bolometer and PCDs through the Stevenson-Wydler Gift Program at Sandia National Laboratories. We thank Mark Perreault, Steven Exelby, Drew Packard, Nick Ramey, and Cayetano Wagner for their experimental assistance. The EUV camera was purchased with funds from a Faculty Development Grant from the US Nuclear Regulatory Commission. The fast framing camera was supported by a 427 DURIP, AFOSR Grant No. FA9550-15-1-0419. This work was supported by the National Science Foundation under Grant No. PHY-1705418 and the DOE under Grant No. DE-SC0012328 of the NSF-DOE Partnership in Basic Plasma Science and Engineering, the LDRD and Campus Executives Programs at Sandia National Laboratories (Project 20-9240), and the NNSA Stewardship Sciences Academic Programs under DOE Cooperative Agreement DE-NA0003764.

References

[1] J. E. Bailey, T. Nagayama, G. P. Loisel, G. A. Rochau, C. Blancard, J. Colgan, P. Cosse, G. Faussurier, C. J. Fontes, F. Gilleron, I. Golovkin, S. B. Hansen, C. A. Iglesias, D. P. Kilcrease, J. J. MacFarlane, R. C. Mancini, S. N. Nahar, C. Orban, J.-C. Pain, A. K. Pradhan, M. Sherrill, and B. G. Wilson, "A higher-than-predicted measurement of iron opacity at solar interior temperatures," *Nature*, vol. 517, pp. 56 EP –, Dec 2014. [Online]. Available: http://dx.doi.org/10.1038/nature14048

[2] G. A. Rochau, J. E. Bailey, G. A. Chandler, G. Cooper, G. S. Dunham, P. W. Lake, R. J. Leeper, R. W. Lemke, T. A. Mehlhorn, A. Nikroo, K. J. Peterson, C. L. Ruiz, D. G. Schroen, S. A. Slutz, D. Steinman, W. A. Stygar, and W. Varnum, "High performance capsule implosions driven by the Z-pinch dynamic hohlraum," *Plasma Physics and Controlled Fusion*, vol. 49, no. 12B, p. B591, 2007. [Online]. Available: http://stacks.iop.org/0741-3335/49/i=12B/a=S55

[3] S. A. Slutz, M. C. Herrmann, R. A. Vesey, A. B. Sefkow, D. B. Sinars, D. C. Rovang, K. J. Peterson, and M. E. Cuneo, "Pulsed-power-driven cylindrical liner implosions of laser preheated fuel magnetized with an axial field," *Physics of Plasmas*, vol. 17, no. 5, p. 056303, 2010. [Online]. Available: https://doi.org/10.1063/1.3333505

[4] S. A. Slutz and R. A. Vesey, "High-Gain Magnetized Inertial Fusion," *Phys. Rev. Lett.*, vol. 108, p. 025003, Jan 2012. [Online]. Available: https://link.aps.org/doi/10.1103/PhysRevLett.108.025003

[5] M. E. Cuneo, M. C. Herrmann, D. B. Sinars, S. A. Slutz, W. A. Stygar, R. A. Vesey, A. B. Sefkow, G. A. Rochau, G. A. Chandler, J. E. Bailey, J. L. Porter, R. D. McBride, D. C. Rovang, M. G. Mazarakis, E. P. Yu, D. C. Lamppa, K. J. Peterson, C. Nakhleh, S. B. Hansen, A. J. Lopez, M. E. Savage, C. A. Jennings, M. R. Martin, R. W. Lemke, B. W. Atherton, I. C. Smith, P. K. Rambo, M. Jones, M. R. Lopez, P. J. Christenson, M. A. Sweeney, B. Jones, L. A. McPherson, E. Harding, M. R. Gomez, P. F. Knapp, T. J. Awe, R. J. Leeper, C. L. Ruiz, G. W. Cooper, K. D. Hahn, J. McKenney, A. C. Owen, G. R. McKee, G. T. Leifeste, D. J. Ampleford, E. M. Waisman, A. Harvey-Thompson, R. J. Kaye, M. H. Hess, S. E. Rosenthal, and M. K. Matzen, "Magnetically Driven Implosions for Inertial Confinement Fusion at Sandia National Laboratories," *IEEE Transactions on Plasma Science*, vol. 40, no. 12, pp. 3222–3245, 2012.

[6] M. R. Gomez, S. A. Slutz, A. B. Sefkow, D. B. Sinars, K. D. Hahn, S. B. Hansen, E. C. Harding, P. F. Knapp, P. F. Schmit, C. A. Jennings, T. J. Awe, M. Geissel, D. C. Rovang, G. A. Chandler, G. W. Cooper, M. E. Cuneo, A. J. Harvey-Thompson, M. C. Herrmann, M. H. Hess, O. Johns, D. C. Lamppa, M. R. Martin, R. D. McBride, K. J. Peterson, J. L. Porter, G. K. Robertson, G. A. Rochau, C. L. Ruiz, M. E. Savage, I. C. Smith, W. A. Stygar, and R. A. Vesey, "Experimental Demonstration of Fusion-Relevant Conditions in Magnetized Liner Inertial Fusion," *Phys. Rev. Lett.*, vol. 113, p. 155003, Oct 2014. [Online]. Available: http://link.aps.org/doi/10.1103/PhysRevLett.113.155003

[7] R. M. Gilgenbach, M. R. Gomez, J. C. Zier, W. W. Tang, D. M. French, Y. Y. Lau, M. G. Mazarakis, M. E. Cuneo, M. D. Johnston, B. V. Oliver, T. A. Mehlhorn, A. A. Kim, and V. A. Sinebryukhov, "MAIZE: a 1 MA LTD-Driven Z-Pinch at The University of Michigan," *AIP*

Conference Proceedings, vol. 1088, no. 1, pp. 259–262, Jan 2009. [Online]. Available: http://aip.scitation.org/doi/abs/10.1063/1.3079742

[8] A. A. Kim, M. G. Mazarakis, V. A. Sinebryukhov, B. M. Kovalchuk, V. A. Visir, S. N. Volkov, F. Bayol, A. N. Bastrikov, V. G. Durakov, S. V. Frolov, V. M. Alexeenko, D. H. McDaniel, W. E. Fowler, K. LeChien, C. Olson, W. A. Stygar, K. W. Struve, J. Porter, and R. M. Gilgenbach, "Development and tests of fast 1-MA linear transformer driver stages," *Phys. Rev. ST Accel. Beams*, vol. 12, p. 050402, May 2009. [Online]. Available: https://link.aps.org/doi/10.1103/PhysRevSTAB.12.050402

[9] D. A. Yager-Elorriaga, P. Zhang, A. M. Steiner, N. M. Jordan, Y. Y. Lau, and R. M. Gilgenbach, "Seeded and unseeded helical modes in magnetized, non-imploding cylindrical liner-plasmas," *Physics of Plasmas*, vol. 23, no. 10, p. 101205, Oct 2016. [Online]. Available: https://doi.org/10.1063/1.4965240

[10] D. A. Yager-Elorriaga, P. Zhang, A. M. Steiner, N. M. Jordan, P. C. Campbell, Y. Y. Lau, and R. M. Gilgenbach, "Discrete helical modes in imploding and exploding cylindrical, magnetized liners," *Physics of Plasmas*, vol. 23, no. 12, p. 124502, 2016. [Online]. Available: https://doi.org/10.1063/1.4969082

[11] A. S. Safronova, V. L. Kantsyrev, M. E. Weller, V. V. Shlyaptseva, I. K. Shrestha, M. Y. Lorance, M. T. Schmidt-Petersen, A. Stafford, M. C. Cooper, A. M. Steiner, D. A. Yager-Elorriaga, S. G. Patel, N. M. Jordan, R. M. Gilgenbach, and A. S. Chuvatin, "Double and Single Planar Wire Arrays on University-Scale Low-Impedance LTD Generator," *IEEE Transactions on Plasma Science*, vol. 44, no. 4, pp. 432–440, 2016.

[12] A. M. Steiner, D. A. Yager-Elorriaga, S. G. Patel, N. M. Jordan, R. M. Gilgenbach, A. S. Safronova, V. L. Kantsyrev, V. V. Shlyaptseva, I. Shrestha, and M. T. Schmidt-Petersen, "Determination of plasma pinch time and effective current radius of double planar wire array implosions from current measurements on a 1-MA linear transformer driver," *Physics of Plasmas*, vol. 23, no. 10, p. 101206, 2016. [Online]. Available: https://doi.org/10.1063/1.4965241

[13] B. M. Kovalchuk, A. A. Kim, E. V. Kumpjak, N. V. Zoi, J. P. Corley, D. L. Johnson, and K. W. Struve, "Multi gap switch for Marx generators," in *IEEE Conference Record - Abstracts. PPPS-2001 Pulsed Power Plasma Science 2001. 28th IEEE International Conference on Plasma Science and 13th IEEE International Pulsed Power Conference (Cat. No.01CH37*, 2001, p. 539.

[14] D. C. Rovang, D. C. Lamppa, M. E. Cuneo, A. C. Owen, J. McKenney, D. W. Johnson, S. Radovich, R. J. Kaye, R. D. McBride, C. S. Alexander, T. J. Awe, S. A. Slutz, A. B. Sefkow, T. A. Haill, P. A. Jones, J. W. Argo, D. G. Dalton, G. K. Robertson, E. M. Waisman, D. B. Sinars, J. Meissner, M. Milhous, D. N. Nguyen, and C. H. Mielke, "Pulsed-coil magnet systems for applying uniform 10–30 T fields to centimeter-scale targets on Sandia's Z facility," *Review of Scientific Instruments*, vol. 85, no. 12, p. 124701, 2014. [Online]. Available: https://doi.org/10.1063/1.4902566

[15] E. M. Waisman, R. D. McBride, M. E. Cuneo, D. F. Wenger, W. E. Fowler, W. A. Johnson, L. I. Basilio, R. S. Coats, C. A. Jennings, D. B. Sinars, R. A. Vesey, B. Jones, D. J. Ampleford, R. W. Lemke, M. R. Martin, P. C. Schrafel, S. A. Lewis, J. K. Moore, M. E. Savage, and W. A. Stygar, "Voltage measurements at the vacuum post-hole convolute of the Z pulsed-power accelerator," *Phys. Rev. ST Accel. Beams*, vol. 17, p. 120401, Dec 2014. [Online]. Available: https://link.aps.org/doi/10.1103/PhysRevSTAB.17.120401

[16] O. A. Hurricane, "Optimized minimal inductance transmission line configuration for Z-pinch experiments," *Journal of Applied Physics*, vol. 95, no. 8, pp. 4503–4505, 2004. [Online]. Available: https://doi.org/10.1063/1.1687986

[17] J. C. Zier, S. G. Patel, D. M. French, M. R. Gomez, R. M. Gilgenbach, Y. Y. Lau, D. A. Chalenski, A. M. Steiner, M. A. Franzi, I. M. Rittersdorf, M. Weis, M. G. Mazarakis, M. R. Lopez, and M. E. Cuneo, "Plasma instability measurements on planar Al foil loads driven using the MAIZE 1-MA LTD facility," in *2011 Abstracts IEEE International Conference on Plasma Science*, 2011, pp. 1–1.

[18] A. Gerrard and J. M. Burch, *Introduction to Matrix Methods in Optics*, reprint edition ed. Dover Publishers, 2012.

[19] S. N. Bland, D. J. Ampleford, S. C. Bott, S. V. Lebedev, J. B. A. Palmer, S. A. Pikuz, and T. A. Shelkovenko, "Extreme ultraviolet imaging of wire array z-pinch experiments," *Review of Scientific Instruments*, vol. 75, no. 10, pp. 3941–3943, Oct 2004. [Online]. Available: https://doi.org/10.1063/1.1787926

[20] T. C. Wagoner, W. A. Stygar, H. C. Ives, T. L. Gilliland, R. B. Spielman, M. F. Johnson, P. G. Reynolds, J. K. Moore, R. L. Mourning, D. L. Fehl, K. E. Androlewicz, J. E. Bailey, R. S. Broyles, T. A. Dinwoodie, G. L. Donovan, M. E. Dudley, K. D. Hahn, A. A. Kim, J. R. Lee, R. J. Leeper, G. T. Leifeste, J. A. Melville, J. A. Mills, L. P. Mix, W. B. S. Moore, B. P. Peyton, J. L. Porter, G. A. Rochau, G. E. Rochau, M. E. Savage, J. F. Seamen, J. D. Serrano, A. W. Sharpe, R. W. Shoup, J. S. Slopek, C. S. Speas, K. W. Struve, D. M. Van De Valde, and R. M. Woodring, "Differential-output B-dot and D-dot monitors for current and voltage measurements on a 20-MA, 3-MV pulsed-power accelerator," *Phys. Rev. ST Accel. Beams*, vol. 11, p. 100401, Oct 2008. [Online]. Available: https://link.aps.org/doi/10.1103/PhysRevSTAB.11.100401

[21] I. H. Hutchinson, *Principles of Plasma Diagnostics*, 2nd ed. Cambridge University Press, 2002.

[22] T. A. Shelkovenko and D. A. Chalenski and K. M. Chandler and J. D. Douglass and J. B. Greenly and D. A. Hammer and B. R. Kusse and R. D. McBride and S. A. Pikuz, "Diagnostics on the cobra pulsed power generator," *Review of Scientific Instruments*, vol. 77, no. 10, p. 10F521, 2006. [Online]. Available: https://doi.org/10.1063/1.2229189

[23] R. D. McBride, W. A. Stygar, M. E. Cuneo, D. B. Sinars, M. G. Mazarakis, J. J. Leckbee, M. E. Savage, B. T. Hutsel, M. L. Kiefer, B. V. Oliver, M. R. Gomez, D. A. Yager-Elorriaga, S. G. Patel, B. M. Kovalchuk, A. A. Kim, P.-A. Gourdain, S. N. Bland, S. Portillo, S. C. Bott-Suzuki, F. N. Beg, Y. Maron, R. B. Spielman, D. V. Rose, D. R. Welch, J. C. Zier, J. W. Schumer, J. B. Greenly, A. M. Covington, A. M. Steiner, P. C. Campbell, S. M. Miller, J. M. Woolstrum, N. B. Ramey, N. M. Jordan, Y. Y. Lau, and R. M. Gilgenbach, "A Primer on Pulsed Power and Linear Transformer Drivers for High Energy Density Physics Applications," *IEEE Transactions on Plasma Science*, vol. 46, this issue, 2018.

[24] M. G. Haines, "The Inverse Skin Effect," *Proceedings of the Physical Society*, vol. 74, no. 5, p. 576, 1959. [Online]. Available: http://stacks.iop.org/0370-1328/74/i=5/a=310

[25] J. Greenly, C. Seyler, and X. Zhao, "Pulsed-power driven reconnection and the inverse skin effect," *Paper JP8 97, Bull. Am. Phys. Soc.*, vol. 59, p. 133, 2014. [Online]. Available: http://meetings.aps.org/link/BAPS.2014.DPP.JP8.97

[26] S. A. Pikuz, T. A. Shelkovenko, and D. A. Hammer, "X-pinch. Part I," *Plasma Physics Reports*, vol. 41, no. 4, pp. 291–342, Apr 2015. [Online]. Available: https://doi.org/10.1134/S1063780X15040054

[27] S. A. Pikuz, T. A. Shelkovenko, and D. A. v. Hammer, "X-pinch. Part II," *Plasma Physics Reports*, vol. 41, no. 6, pp. 445–491, Jun 2015. [Online]. Available: https://doi.org/10.1134/S1063780X15060045